Eur. Phys. J. B **6**, 167–181 (1998)

THE EUROPEAN PHYSICAL JOURNAL B

Zero temperature phase transitions in spin-ladders: Phase diagram and dynamical studies of $Cu_2(C_5H_{12}N_2)_2Cl_4$

G. Chaboussant[1,a], M.-H. Julien[1,b], Y. Fagot-Revurat[1,c], M. Hanson[1], L.P. Lévy[1,2,d], C. Berthier[1,3], M. Horvatić[1], and O. Piovesana[4]

[1] Grenoble High Magnetic Field Laboratory, CNRS and MPI-FKF, BP 166, 38042 Grenoble, France
[2] Institut Universitaire de France and Université Joseph Fourier, BP 53, 38400 St Martin d'Hères, France
[3] Laboratoire de Spectrométrie Physique, Université Joseph Fourier, BP 87, 38402 St Martin d'Hères, France
[4] Dipartimento di Chimica, Università di Perugia, 06100 Perugia, Italy

Received: 13 March 1998 / Received in final form and Accepted: 21 July 1998

Abstract. In a magnetic field, spin-ladders undergo two zero-temperature phase transitions at the critical fields H_{c1} and H_{c2}. An experimental review of static and dynamical properties of spin-ladders close to these critical points is presented. The scaling functions, universal to all quantum critical points in one-dimension, are extracted from (a) the thermodynamic quantities (magnetization) and (b) the dynamical functions (NMR relaxation). A simple mapping of strongly coupled spin ladders in a magnetic field on the exactly solvable XXZ model enables to make detailed fits and gives an overall understanding of a broad class of quantum magnets in their gapless phase (between H_{c1} and H_{c2}). In this phase, the low temperature divergence of the NMR relaxation demonstrates its Luttinger liquid nature as well as the novel quantum critical regime at higher temperature. The general behavior close these quantum critical points can be tied to known models of quantum magnetism.

PACS. 75.10.Jm Quantized spin models – 75.40.-s Critical-points effects, specific heats, short range order – 76.60.-k Nuclear magnetic resonance and relaxation

1 Introduction

It is well known that long-range order is destroyed by quantum fluctuations in one-dimensional antiferromagnets. If the importance of quantum effects is ubiquitous in one-dimension, a wide variety of ground states can nevertheless be found in nature. Some systems have a continuum of low energy modes, some have an energy gap above a unique ground state, other dimerize. Where do these differences come from? In simple terms, the role of quantum effects is simply to "connect" different classical ground states (for example the Néel states $|\uparrow,\downarrow,\uparrow,\downarrow,\ldots\rangle$ and $|\downarrow,\uparrow,\downarrow,\uparrow,\ldots\rangle$) by tunneling processes. Depending of the strength of the tunneling matrix elements, which can usually be measured by a coupling constant g, the system will be more or less localized around a classical ground states. As g is varied, the system can delocalize at a critical value g_c. When the system delocalizes in spin space, the ground state becomes a rotationally invariant singlet and in all the cases which will be considered here, an energy gap Δ appears simultaneously in the energy spectrum. Many physical aspects determine the strength of quantum fluctuations. The integer or half-integer nature of the spin considered modify drastically selections rules for quantum-processes [1]. This is why integer-spin chains for which g exceed g_c have an energy gap, while half-integer spin-chains remain gapless ($g \leq g_c$). Other physical parameters (exchange constants, applied magnetic fields) also enter in the precise determination of the coupling strength g. Systems for which the coupling constant can be continuously varied by an experimentally controllable parameter, such as a magnetic field, are rare. In this paper we review a few 1D antiferromagnets where such zero temperature critical points have been observed, with a particular emphasis on $Cu_2(C_5H_{12}N_2)_2Cl_4$ (also known as CuHpCl) [2–4], a spin-ladder compound, where a complete set of experiments exist.

At a quantum critical point [5–9], the system switches from one ground state into another. Specifically when $g \leq g_c$, antiferromagnetic correlation functions decay as power laws and the system is nearly ordered. When g is increased above g_c, a gap opens up and the range of antiferromagnetic correlation become finite, of the order

[a] *Present address:* ISIS Facility, Rutherford Appleton Laboratory, Didcot, Oxon OX11 0QX, United Kingdom.
[b] *Present address:* Dpt. of Physics "A. Volta" Universita di Pavia, Via Bassi 6, 27100 Pavia, Italy.
[c] *Present address:* Physikalisches Institut, Universität Stuttgart, Pfaffenwaldring 57, 70550 Stuttgart, Germany.
[d] e-mail: `levy@grenet.fr`

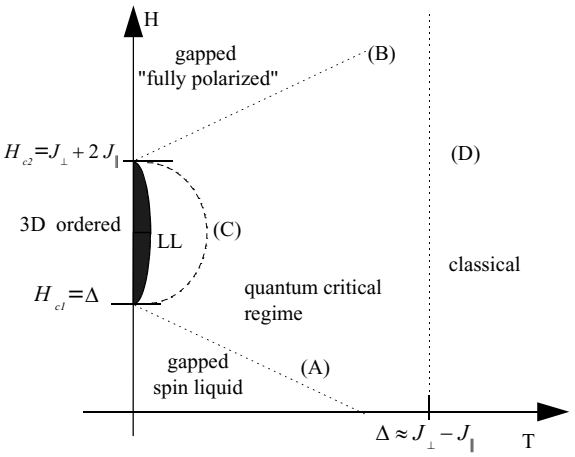

Fig. 1. Phase diagram of spin-ladders in a magnetic field. The magnetic field (vertical axis), can be thought as a tuning parameter for the quantum coupling constant g. Below $H_{c1} \Leftrightarrow g_c$, the coupling constant g exceeds g_c ($H \leq H_{c1} \Leftrightarrow g \geq g_c$). This phase has a singlet ground state and an energy gap. Above H_{c1}, the coupling constant g drops below g_c: the phase is magnetic and gapless and belongs to the same universality class as the Heisenberg XXZ model. The dotted lines represent the crossover lines where $\xi_g \simeq \xi_T$ separating two quantum regimes just described (where ξ_g is the relevant quantum correlation length) from the quantum critical regime dominated by ξ_T. For the system discussed in this paper the quantum critical behavior at the upper critical field H_{c2} is similar and will be discussed in the next sections. The shaded area between critical fields is a 3D ordered phase stabilized by transverse interactions (see Sect. 5).

of $\xi_g \simeq a/|g-g_c|$ (a is the lattice constant). In the vicinity of g_c, one has to go to relatively long lengthscale, exceeding ξ_g to be able to tell in which phase the system is. In other words, the nature of the ground state is manifest only at long lengthscale. At finite temperature spin-flip processes become possible. They cut spin-correlations off at a lengthscale ξ_T which can be estimated in the quantum-disordered phase ($g \geq g_c$) as the mean distance between excitations. Since their energies are higher than the energy gap $\Delta \simeq 1/|g-g_c|$ above the ground state, their density is activated. Hence when $k_BT < \Delta$, the mean distance between excitations ξ_T greatly exceed ξ_g and thermal fluctuations are not really relevant. On the other hand, when $k_BT \geq \Delta$, their density is governed by the relative value of $k_BT - \Delta$ compared to the bandwidth of the triplet excitations. When Δ is small compared to k_BT and this bandwidth, ξ_g exceeds very rapidly ξ_T. In this case, the density of excitations are determined by k_BT *alone* which become the only relevant energy scale. In this limit, dynamical properties are similar to those of a simple paramagnet ($1/T_1 \rightarrow cst$) while thermodynamics quantities remain nontrivial. This regime is (improperly) named the *quantum critical regime*, because most properties are determined by the single lengthscale ξ_T as in ordinary phase transitions.

To summarize, there are two-relevant lengthscales at a quantum critical point, the quantum correlation length ξ_g and the thermal length ξ_T. Depending on their relative values, different regimes exists. They are represented graphically in Figure 1, on the H-T phase diagram appropriate to spin-ladders. The regions dominated by quantum effects are (a) the gapped spin-liquid phase below line A, (b) the XXZ or Luttinger liquid phase to the left of line C and (c) the gapped polarized phase above line B. The quantum critical region is found to the right of these crossover line and extends down to $T = 0$ at the critical fields H_{c1} and H_{c2}. Each regime will clearly be identified using thermodynamic and $1/T_1$ NMR relaxation measurements which allow to place precisely the crossover lines on this phase diagram.

The differents sections are organized as follows: a brief description of several families of gapped antiferromagnets having an H-T phase diagram similar to the one shown in Figure 1 can be found in Section 2. A description of the structure and the interactions relevant to CuHpCl, the 1D ladder system chosen for our case study, is given in Section 3. A mapping of strongly coupled ladder in a magnetic field onto the XXZ Heisenberg model is introduced in Section 4. It is used throughout the rest of the paper to fit and interpret experimental data. In Section 5, the different phases shown in Figure 1 are identified using high-field magnetization data. The XXZ model is used to fit the low temperature data and to give a physical model for the ordered phase observed between H_{c1} and H_{c2}. Section 6 is devoted to the dynamical processes entering in the NMR relaxation. The different regimes decribed in Figure 1 are presented in Section 7 through T_1^{-1} measurements across the entire phase diagram. The Luttinger liquid behavior between H_{c1} and H_{c2} is clearly seen for the first time and compared to the XXZ models. Finally the first scaling analysis for a 1D quantum critical point is presented in Section 8 and the paper concludes with some new perspectives.

2 Gapped 1D antiferromagnets: a broad universality class

There are three known families of quasi 1D materials belonging to the same universality class, with an H-T phase diagram similar to Figure 1. They can all be described by the same quantum-field theory, the O(3) non-linear σ-model [1,11,12] in a magnetic field. Their excitation spectrum [13] in a weak magnetic field is represented in Figure 2. The lower critical field H_{c1}, is reached when the lowest energy gap Δ_- vanishes. The upper critical field H_{c2} is usually reached when the highest energy state of the $\epsilon_-(q)$ branch is below the singlet energy. An approximate representation of their singlet ground-states are represented in Figure 3.

The know families of 1D antiferromagnets in this universality class are:

(i) Quasi 1D-antiferromagnetic compounds with two alternating exchange constants J_1 and J_2 have been known for over two decades to have a gap (Fig. 3a). For spin-1/2 alternating chains, the spectrum

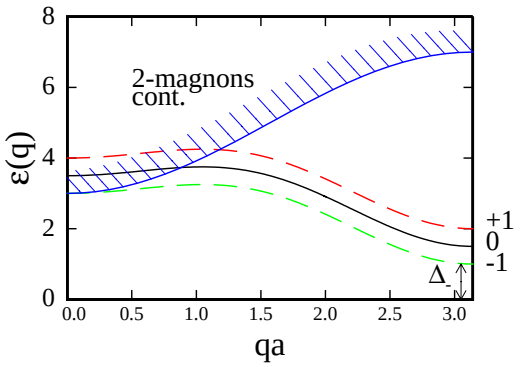

Fig. 2. The lowest lying excitations form a triplet branch, split by the Zeeman field, or other anisotropic forces. They are separated from a unique singlet ground state by energy gaps $\Delta_+, \Delta_0, \Delta_-$. In absence of anisotropies, they are split by the Zeeman energy, $\Delta_\pm = \Delta_0 \pm g\mu_B H$. The shape of the dispersion relation across the Brillouin zone depends on the exchange interactions specific to each 1D system. In particular, the energy gap may be at $qa = \pi$ (S=1 chains, ladders) or at $q = 0$ (dimerized chains with sufficiently large antiferromagnetic second-neighbor exchange). Similarly, a two-"magnons" continuum may intersect the triplet branch and have a lower energy in some region of the Brillouin zone. In this universality class, there are no singlet states in the gap.

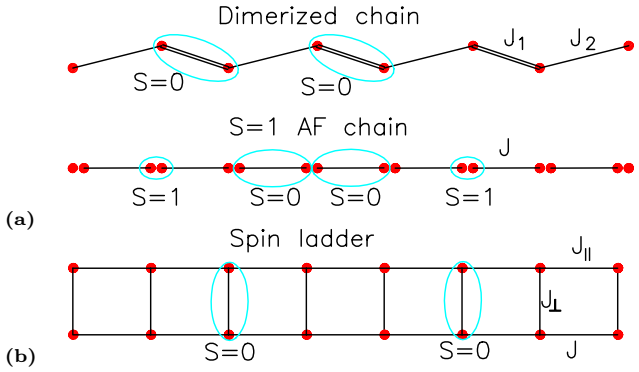

Fig. 3. Three families of gapped antiferromagnets. (a) Dimerized chains: the antiferromagnetic bond J_1 dominates J_2. Singlet valence bonds are preferentially localized on these bonds. Middle, integer spin chains. The ground state can also be viewed as a product of valence bonds [14], by decomposing each spin 1 in two spin-1/2 and forming valence bonds with the pair of spin-1/2 at the extremity of each bonds (valence bond solid). (b) Spin ladders. In the strong coupling limit ($J_\perp \gg J_\parallel$), singlet bonds are localized on the rungs of the ladder.

is identical to Figure 2 and in the strong coupling limit ($J_1 \gg J_2$), the energy gap is $\Delta \approx J_1 - \frac{J_2}{2} - \frac{3}{8}\frac{J_2^2}{J_1}$. Very nice thermodynamic studies [15] of $Cu(NO_3)_2.2.5H_2O$ have identified the existence of two critical fields $H_{c1} \approx J_1 - J_2/2 \simeq 2.8$ T and $H_{c2} \equiv 2J_1 \simeq 4.5$ T. In spite of the modest value of H_{c1} and H_{c2}, dynamical properties close to these critical points have never been thoroughly mapped out neither by NMR relaxation measurements nor by neutron scattering. Considering the interest in quantum phase-transition, this interesting compound should be revisited.

(ii) Spin-1 Heisenberg antiferromagnetic chains [1] with a sufficiently weak planar anisotropy have in zero magnetic field a triplet excitation branch separated by an energy gap $\Delta \approx 0.41 \times J$ from the unique singlet ground state. The most thoroughly studied compound in this family is NENP [16]. Because of the presence of a planar anisotropy, this system has three different lower critical fields (9.8, 13.3 and 14 T) [17, 18] depending on the orientation of the field with respect to the anisotropy axes. The upper critical field which has not been measured should exceed 86 Tesla. Thermodynamic and dynamical measurements [19] have been carried out at the lower critical field and provide very valuable insight on zero-temperature phase transitions.

(iii) Spin-ladders are quasi-1D structures where a finite number of antiferromagnetic chains are coupled by a transverse antiferromagnetic exchange. Ladders with an odd-number of coupled chains are gapless and belong to the same universality class as the spin-1/2 Heisenberg chain [20]. On the other hand, spin-1/2 ladders with an even number of legs are gapped and form a singlet ground-state with short ranged spin correlations (spin-liquid). While several compounds with ladder-like magnetic structure exist [21,22], the only system where the quantum critical point H_{c1} is experimentally accessible is CuHpCl, a coordination compound made up by stacking binuclear molecules in a ladder structure [23]. Thermodynamic [2,30] and dynamic quantities [3,4] have been measured over the entire phase diagram and give a relatively complete experimental picture of a zero-temperature phase transition.

We now describe its structure, and the relevant magnetic interactions in this material.

3 CuHpCl, a 1D spin ladder in the strong coupling limit

The molecular unit is a binuclear structure with two Cu^{2+} ions (spin 1/2) each lying in a middle of two parallel distorted square-structures [23]. At the vertices of each square, one finds two chlorine and two nitrogen ions as depicted in the top of Figure 4. There are two super-exchange paths through the chlorine ions Cl_1 and Cl_2 bridging the copper ions. However, the p_z orbitals of the chlorine ions are nearly orthogonal to the Cu^{2+} d_{xy} orbital. The resulting exchange constant between the copper ions $J_\perp \approx 13.5$ K, is found to be weaker than in other materials with similar Cu−Cu distance. The organic rings, on the outside of the ionic-core just described, contribute further to the delocalization of the unpaired Cu^{2+} orbital. Each molecular unit stacks up in the [101] direction

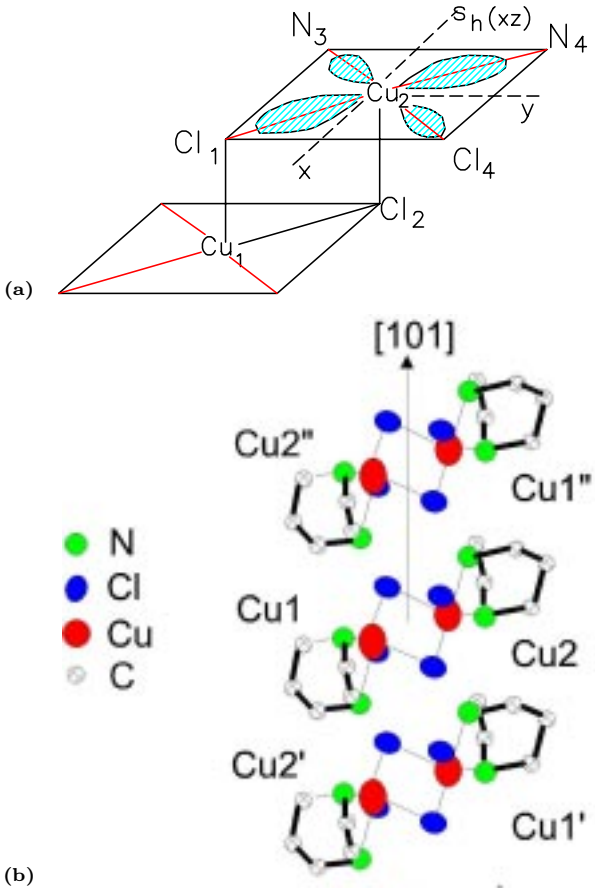

Fig. 4. (a) Representation of the parallel plane geometry of the Cu^{2+} orbitals. (b) Stacking of the molecular units in a ladder structure along the [101] axis.

of this $P2_1/c$ molecular crystal (see Fig. 4). In addition to the van-der-Vaals forces, the organic rings allow a weak hydrogen bonding between molecules, along which a super-exchange path can propagate. In spite of the relatively large intermolecular Cu−Cu distance, the orbital overlaps are favorable and lead to an intermolecular-exchange interaction $J_\parallel \approx 2.45$ K along the ladder. Strictly speaking, due to the low symmetry, there are small differences in Cu−Cu distances along the ladder above and below each molecular unit. Because the bridging entities have the same symmetries, these small differences are not expected to modulate significantly the exchange ($J_\parallel$) along the legs. The translational invariance is nevertheless naturally broken, making any additional lattice (spin-Peierls) instabilities less favorable. Comparison of thermodynamic properties to numerical simulations [24] have demonstrated that the other possible magnetic cross-bondings between the legs are weak and need not be considered. On the other hand, it is now clear that there is also a weak inter-ladder super-exchange, probably also mediated by a weak hydrogen bonding between organic rings. If it is not relevant in the gapped phases, it induces at low-T a 3D-ordered phase in the gapless region between H_{c1} and H_{c2} [30]. While this phase has been observed in specific heat measurements, its actual structure has not been determined experimentally.

4 Hamiltonian representations of strongly-coupled spin-ladders

For most purposes, it will be sufficient to consider a quasi-1D ladder Hamiltonian in a magnetic field $\mathcal{H} = \mathcal{H}_1 + \mathcal{H}_2 + \mathcal{H}_Z$, where

$$\mathcal{H}_1 = J_\perp \sum_{i=1}^{N} \boldsymbol{S}_{2i-1} \cdot \boldsymbol{S}_{2i} \tag{1}$$

$$\mathcal{H}_2 = J_\parallel \sum_{i=1}^{2N} \boldsymbol{S}_i \cdot \boldsymbol{S}_{i+2}, \tag{2}$$

(even spins are on one leg and odd spins are on the other). The weak g-factor anisotropy ($g_\perp \approx 2.03, g_\parallel \approx 2.11$) observed in EPR measurements [2] may be retained in the Zeeman Hamiltonian, $\mathcal{H}_Z = \sum_{i=1,\alpha}^{2N} g_\alpha \mu_B S_i^\alpha H_\alpha$. In the strong coupling limit ($J_\perp \gg J_\parallel$), it is possible to give a straightforward description of the low-energy states in a magnetic field, treating $\mathcal{H}_2$ as a perturbation [25,26]. The eigenstates of $\mathcal{H}_1 + \mathcal{H}_Z$ which describes isolated dimers in a magnetic field, are built from the singlet  (valence bonding) and triplets  ,  ,  (antibonding) on each rung. Since we are interested in the critical region, where the Zeeman energy is of the order of $J_\perp$, it is legitimate to project $\mathcal{H}_2$ on the restricted Hilbert space generated by the lowest dimers states,  and . The matrix elements of $\mathcal{H}_2$ between neighboring dimers can be represented on this subspace by a 2×2 matrix, which is expressed in second-quantized notation as

$$\mathcal{H}_2^{eff} = \frac{J_\parallel}{2} \sum_{r=1}^{N} \left(t_r^\dagger t_{r+1} + t_r t_{r+1}^\dagger + n_r n_{r+1} \right). \tag{3}$$

The fermionic operator $t^\dagger$ creates the triplet state  on bond $r \equiv [2i, 2i+1]$ (only one triplet per bond is allowed), while t destroys a triplet, leaving a singlet on bond r. The operator $n_r \equiv t^\dagger{}_r t_r$ counts the triplet occupation of bond r. In the fermion language, the first two terms represent the kinetic energy while the last term is a short range repulsion between fermions. Since S^2 and S_z are good quantum numbers ($\boldsymbol{S}$ is the total spin), it is convenient to divide the Hilbert space into sectors with a given value of S_z. In the restricted Hilbert space, each sector specifies the total fermionic occupation since

$$S_z = \sum_r n_r. \tag{4}$$

The singlet sector is not coupled by $\mathcal{H}_2^{eff}$ and the singlet eigenstate remains the dimer product $|S=0\rangle = |$  $\ldots\rangle$ with energy $E_0 = -\frac{3}{4} N J_\perp$. This ground state energy

may be compared to a serie expansion[1] in $J_\parallel/J_\perp$ [27]. For the parameters appropriate to CuHpCl, the corresponding singlet energy is only 1.6% lower than in the previous estimate. The reduction of $\mathcal{H}_2$ to equation 3 is therefore appropriate to CuHpCl, at least for qualitative answers.

In the $S = 1$ (1-fermion) sector, the Hamiltonian $\mathcal{H}_2^{eff}$ can also be diagonalized in Fourier space, since the interaction term $n_r n_{r+1}$ does not contribute. The dispersion relation of this triplet state is,

$$E_{S_z=-1}(q) = J_\perp - g_z\mu_B H + J_\parallel \cos(qa), \quad (7)$$

$$|1,q\rangle = \sum_r \exp(iqr)|\ldots_{r-1}\ r\ _{r+1}\ldots\rangle. \quad (8)$$

For fields below $g_z\mu_B H_{c1} \approx \Delta_0 = J_\perp - J_\parallel$, there is an energy gap $\Delta_- = \Delta_0 - g_z\mu_B H$ between the singlet and the $q = \pi/a$ minimum of the triplet branch, as shown in Figure 2. For fields above H_{c1} or temperatures above the gap Δ_-/k_B, it is necessary to explore the energy spectrum of $\mathcal{H}_2$ at finite fermion density. In the low-energy sector of the Hilbert space ($|\ ,\ _{-1}$), a finite fermion density raises the energy of $\mathcal{H}_1 + H_z$ with respect to the ground state by an amount proportional to the triplet (fermion) density

$$\delta E = (J_\perp - g_z\mu_B H)\sum n_r. \quad (9)$$

In other words, $\mu \equiv J_\perp - g_z\mu_B H$ acts as the chemical potential for the triplets.

The low energy spectrum of $\mathcal{H}_2^{eff}$ can be described *exactly* on the restricted Hilbert space: equation (3) can be recognized as the fermion representation of the $S = \frac{1}{2}$ XXZ Heisenberg model

$$\mathcal{H}_{eff} = J_\parallel \sum_i \left(S_r^x S_{r+1}^x + S_r^y S_{r+1}^y + \frac{1}{2} S_r^z S_{r+1}^z \right) + H_{eff} \sum_r S_r^z + N\frac{J_\perp}{8}, \quad (10)$$

in an effective field

$$H_{eff} = J_\perp + \frac{J_\parallel}{2} - g_z\mu_B H. \quad (11)$$

H_{eff} is zero at the midpoint between $H_{c1} = J_\perp - J_\parallel$ and the upper critical field $H_{c2} \equiv J_\perp + 2J_\parallel$ [2]. The spin eigenstates of this effective Hamiltonian are a representation of the triplet-singlet subspace ($|\uparrow\rangle \equiv \ _{-1}, |\downarrow\rangle \equiv |\ $) on each rung and have nothing to do with the original spin-1/2. In this model, the excitations which carry $\hbar/2$ angular momentum (spinons), have a semionic character, *i.e.* can only be observed in pairs. In non-zero effective fields ($H_{eff} \neq 0$) the longitudinal and transverse excitations must be distinguished. The continuous spectrum of transverse excitations (1-magnon or 2-spinons) is represented in Figure 5 at two different magnetic fields. At fields just above H_{c1} (Fig. 5a) a new minimum in the spectrum develops at $Q_\sigma a = \pi\sigma$, where $\sigma = M(H_{eff})/M_{sat}$ is the spin-polarization of the XXZ-model in an effective field H_{eff}. The lower critical field $H \approx H_{c1}$ correspond to the saturation field of the XXZ model, $H_{eff}^{sat} \approx 3J_\parallel/2$: the spin-polarization σ in H_{eff}^{sat} is -1 and the ladder magnetization m is zero. Just above H_{c1}, the soft modes at π/a and Q_σ are very close: the spin stiffness $\rho_s \propto (1+\sigma) \propto m$ goes to zero and a large low-energy spectral weight exists close to the antiferromagnetic point. The situation is quite different close to $H_{eff} = 0$ (*i.e.* half-way between H_{c1} and H_{c2}), where the incommensurate wave-vector Q_σ, is close to the zone center (Fig. 5b). For longitudinal fluctuations, the incommensurate minima in the two cases considered are essentially interchanged with respect to transverse fluctuations.

It is useful to "translate" the XXZ incommensurate states just described into the valence bond representation of ladder states. The pictorial images of the incommensurate ground states shown in Figure 6, close to $J_\perp - J_\parallel/4$ and $J_\perp + J_\parallel/2$, are appropriate on short lengthscales

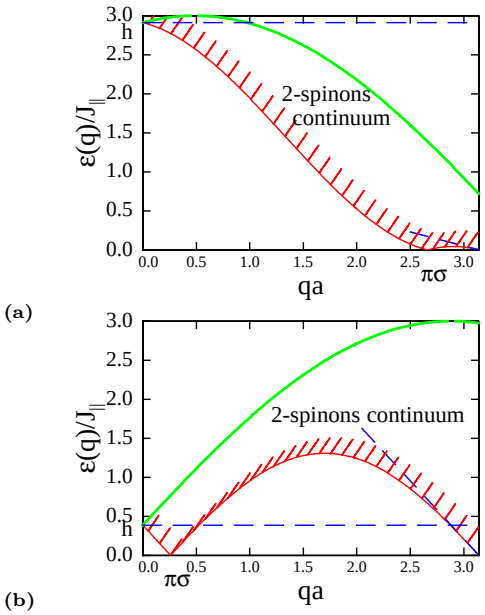

Fig. 5. Energy spectrum of transverse excitations in a magnetic field. (a) $H \geq H_{c1}$, the incommensurate wavevector is close to the antiferromagnetic point. (b) $H \simeq (H_{c1} + H_{c2})/2$, the incommensurate wave-vector is close the zone center. On both plots, the spin-stiffness $\rho_s \propto \sin(\pi - Q_\sigma)$ is the slope of the bottom edge of the spectrum at $q = \pi$.

[1] When the full Hilbert-space is retained, the strong coupling expansion for the singlet ground state reads:

$$|S=0\rangle = |\ \ldots\rangle + \frac{J_\parallel}{J_\perp}\sum_r \cdot \quad (5)$$

$$|\ \ldots\ _{r-1}\ \frac{(\ \ +\ \ )_{r,r+1}}{\sqrt{2}}\ _{r+2}\ldots\rangle + \mathcal{O}\left(\frac{J_\parallel}{J_\perp}\right)^2,$$

$$E_0 = -\frac{3}{4}NJ_\perp\left[1 + \frac{1}{2}\left(\frac{J_\parallel}{J_\perp}\right)^2 + \right] \quad (6)$$

where the same valence bond notation is used for all singlets whether they lie along the legs or the rungs.

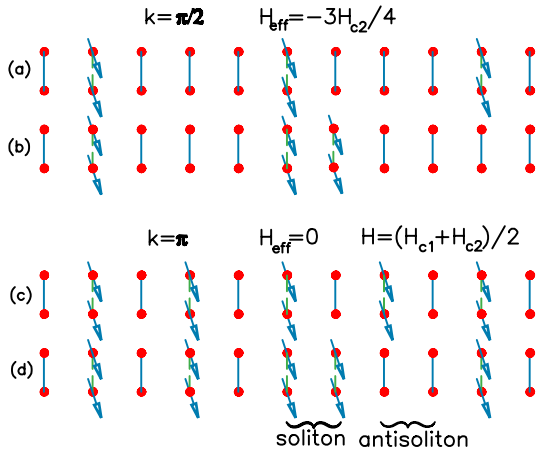

Fig. 6. The $k = \pi/2$ (a) and $k = \pi$ (c) ground states are superposition of the singlet-triplet configurations shown. The wavevector k refers to the wavevector in the XXZ representation. In ladder representation shown, this wavevector is $k/2$. Excitations are built as Bloch wave of the soliton-antisoliton pairs represented on (b) and (d).

(quantum fluctuations destroy the periodicity Q_σ on long lengthscales). Low energy excitation above the ground state are Bloch waves of the soliton-antisoliton defects depicted in Figure 6: this builds a coherent superposition $\alpha|\uparrow\rangle + \beta|\downarrow\rangle_{-1}$ (transverse fluctuation) at wavevector Q_σ.

Since so many exact results are known for the XXZ model, the mapping discussed here will prove to be extremely useful in the analysis experimental data. The high field magnetization of CuHpCl clearly establishes the correspondence with the phase diagram shown in Figure 1.

5 Identification of the different phases with high-field magnetization measurements

The weak g-factor anisotropy and the monoclinic symmetry of this crystal, allow a straightforward determination of the magnetization by torque magnetometry: if the field is applied along the $\hat{z}$ axis, which does not coincide with the principal axes $\hat{a}, \hat{b}, \hat{c}$, the magnetization is not collinear with H, and a torque $\tau \propto M \times H$ can be measured. The magnetization curves of a 100 μg monocrystal have been measured with an ultrasensitive AC torque magnetometer [2,28]. It is straightforward to identify the critical field H_{c1} and H_{c2} from the $T = 0.42$ K magnetization curve shown in Figure 7. Below H_{c1}, the magnetization is thermally activated with an effective gap Δ_- (this is shown in Fig. 8). Similarly, above H_{c2}, the deviation from the saturated magnetization are activated with an energy gap $g_z\mu_B(H - H_{c2})$ (see NMR section). In Appendix A, the energy spectrum of excitations carrying one unit less angular momentum than the fully polarized state are determined. In a ladder, there are two spins in the unit cell, and hence two spin-wave modes. Since the polarized phase is unstable when the lowest energy of these spin-waves drops below the energy of the polarized state, the upper critical

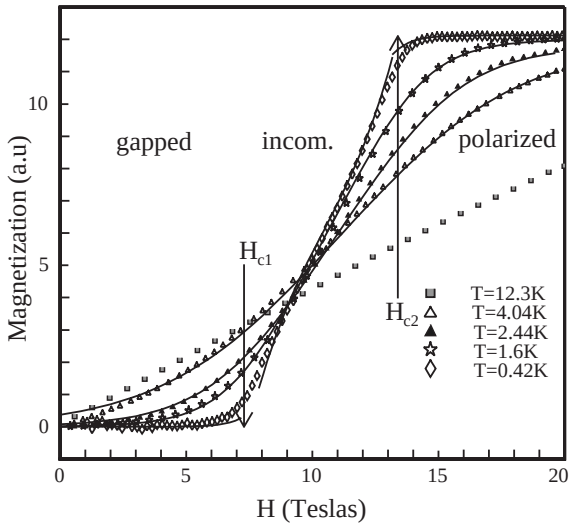

Fig. 7. Magnetization of CuHpCl between 0 and 20 T, at different temperatures. The symbols are experimental data points, while the solid lines are the fits to the XXZ model described in the text, using the procedure outlined in Appendix B. From the lowest temperature curve, two critical fields H_{c1} and H_{c2} are identified. Below H_{c1}, the system is unmagnetizable, *i.e.* forms a singlet ground state separated from $S \neq 0$ excitations. Above H_{c2}, the system is fully polarized. The "incommensurate phase" is between H_{c1} and H_{c2}.

field can be specified exactly

$$g_z\mu_B H_{c2} = J_\perp + 2J_\parallel. \tag{12}$$

The observed behavior of the magnetization in the different field regions coincides precisely with the zero temperature phases specified on the y-axis of Figure 1. Quantitatively, the exchange parameters $J_\perp \approx 13.5\,\mathrm{K}$, $J_\parallel \approx 2.45\,\mathrm{K}$ are most accurately determined from the values of H_{c1} and H_{c2}. $J_\perp$ can be identified independently as the magnetic field at which the NMR relaxation rate is maximum in the high temperature limit (see Sect. 7). These numbers have also been checked against (a) the low and high temperature dependence of the susceptibility [2,29], (b) the gap suppression of the low temperature specific heat and (c) the overall bandwidth ($2J_\parallel$) of the triplet branch ($H = 0$) [30] measured by neutron scattering. In a numerical study of the ladder magnetization, the presence of a weak cross-exchange coupling between legs has also been investigated [24]. The conclusion is that this coupling is weak and if non-zero, ferromagnetic. Considering all the experimental and numerical uncertainties, it seems at present unnecessary to keep any additional exchange coupling in the analysis.

The thermodynamic properties for the XXZ model can be computed exactly by the Bethe Ansatz [32,33] and the magnetization curves have been evaluated numerically using the procedure described in Appendix B. At temperature below $J_\perp$, [35] the results (Fig. 7, solid lines) agree very well with the experimental magnetization.

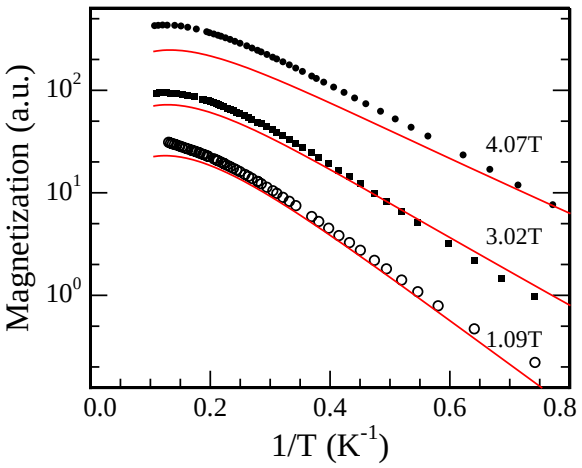

Fig. 8. Magnetization of CuHpCl in the gapped phase as a function of $1/T$, at different magnetic fields. The experimental points are compared to the free fermion model of Troyer (solid lines). A systematic deviation from the free-fermion model is observable when their density becomes significant: this emphasize the role of the short range repulsion between fermions.

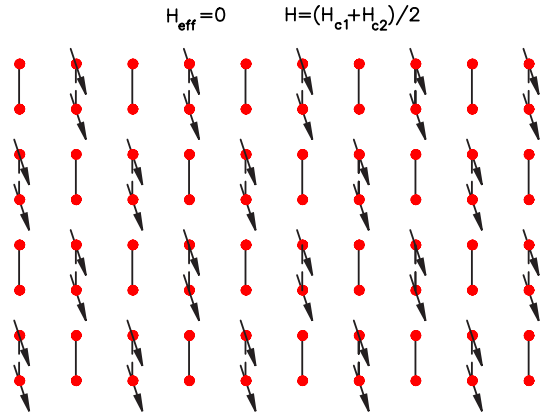

Fig. 9. Suggested ordered dimer-state close to half-filling: triplet and singlet bonds form a 3D antiferromagnetic lattice.

Considering that there are no adjustable parameters, the mapping of strongly-coupled spin-ladders onto the XXZ model appears to be excellent. In particular, the quantum critical behavior of ladders at H_{c1} is acurately reproduced by this model, a point which is emphasized further in Section 8 by constructing explicitly the scaling plots for the magnetization. In the gapped phase, the XXZ mapping progressively loses its validity at small Zeeman splitting (compared to Δ) [35]. In this limit, it is instructive to compare the temperature dependent magnetization to the free-fermion model proposed by Troyer *et al.* [2,34] where

$$\frac{M}{M_{sat}} = \frac{2z(\beta)\sinh(\beta g_z \mu_B H)}{1+[2\cosh\beta g_z\mu_B H]z(\beta)} \qquad (13)$$

and $z(\beta) \approx \exp(-\beta J_\perp) I_0(\beta J_\parallel)$ In this model, the statistical weights are adjusted in order to reproduce the full spin entropy at high temperature, but the nearest-neighbor repulsion is ignored. Figure 8 shows that, at high temperature, the experimental magnetization is systematically higher that inferred by the free-fermion model (solid lines). At finite temperature, interactions between fermions increase the value of the chemical potential (which is negative in the gapped phase, $\mu \geq -|\Delta_-|$). Hence at higher temperature, the effective gap ($|\mu|$) becomes smaller and a higher fermion density is possible. The role of interactions will be further emphasized with the identification of the NMR relaxation processes: the dominant relaxation channel (staggered process) when $H \to H_{c1}$ would not be possible without interactions.

5.1 Ordered phase

Down to $T = 0.1$ K, magnetization curves show no plateaux nor slope changes which could indicate a 3D ordering transition. The 1D models appear to give a precise account of the magnetization at all temperature. On the other hand, small but sharp peaks in the specific heat have been observed above H_{c1} at low temperature [30,31]. After integration of the specific heat at constant field, it is found that the entropy per spin associated to this transition is very small ($< 10^{-2} k_B$/spin). In light of these experimental facts, a *second order* phase transition appears at low-T between H_{c1} and H_{c2}, involving a small change in spin-entropy and no detectable change in magnetization.

When 3D coupling are ignored, the XXZ mapping (Sect. 4) gives a representation in terms of an interacting 1D fluid of spinless fermions (Luttinger liquid). Since there is no magnetization change, the 3D transition takes place at constant fermion density. A very common 3D instability for a 1D Luttinger liquid is a charge density wave ordering. In a valence-bond language, this transition can be viewed as a valence-bond ordering of the 1D $\bullet\!\!\!\!\bullet_{-1}$ states in a 3D-lattice. This would hardly affect the magnetization which measures the density of $\bullet\!\!\!\!\bullet_{-1}$ bonds (fermion density) while the quenching of their kinetic energy would be manifest in the specific heat. For a 3D-charge ordering, repulsive interactions between fermions are usually necessary. Antiferromagnetic superexchange between ladders, introduce very naturally an additional repulsion between fermions on different ladders. This antiferromagnetic super-exchange may be represented by,

$$\mathcal{H}_{inter} = J_{inter} \sum_{\langle k,l \rangle} \boldsymbol{S}_k \cdot \boldsymbol{S}_l \qquad (14)$$

where the sum $\langle k,l \rangle$ is carried over nearest-neighbor spins belonging to different ladders. The physics of a low-T transition should be described by the projection of (14) on the restricted Hilbert space, *i.e.*

$$\mathcal{H}^{eff}_{inter} = -\frac{J_{inter}}{4} \sum_{\langle k,l \rangle} \left(t^\dagger_k t_l + t_k t^\dagger_l - n_k n_l \right), \qquad (15)$$

which has, up to a sign, the same form as $\mathcal{H}^{eff}_2$. A gauge transformation, switching the phase of hopping

operators $t_{2r+1} \to -t_{2r+1}$ every other rungs, restores an effective antiferromagnetic coupling in the spin model. In the spinless fermion model, a transition to a charge density wave state can only be established close to half filling [$H = (H_{c1} + H_{c2})/2$] [36]. It is not known whether this transition persist at low fermion densities. Since this model arise in many context, it will be important to determine its complete phase diagram. Of particular relevance is the commensurate or incommensurate nature of the 3D charge density. The physics of this model is in fact relevant to almost all quasi-1D quantum magnets. For example, in the spin-Peierls compounds $CuGeO_3$, there is also a transition to a 3D incomensurate phase, with no change in total magnetization. At the transition, only the local distribution of magnetization changes [39]. Eßler and Tsvelik [40] have shown that the 3D phonon-couplings present in this family of materials can be represented as a transverse exchange between chains in an effective magnetic Hamiltonian. From the point of view of magnetism, this "charge density wave" ordering cannot be distinguished from a real spin-Peierls transition recently proposed by several authors [31]. It is therefore natural to expect ordered phases with similar structures in all compounds within this universality class.

From the point of view of magnetism, this is an original magnetic state, with a 3D ordered structure of valence bonds. Figure 9 gives a pictorial representation of this state at half-filling ($(H = H_{c1} + H_{c2})/2$). From this discussion, it is clear that further experimental and theoretical studies of the 3D ordering of strongly coupled ladder are called for.

6 Assigment of NMR lines and identification of the dynamical relaxation processes in the gapped phase

NMR is an ideal tool to probe the low-energy dynamics of quantum magnets [3]. When nuclei (here protons) are located at different sites than the electronic spins, the interaction between electronic and nuclear spins are mostly dipolar: the dipolar field $\boldsymbol{h}_{ij}(t)$ produced by the electronic spin i on the nuclear spin j serves a probe for the dynamical properties. The time-averaged z-component $\sum_i \langle h_{ij}^z \rangle$ of this local field shifts the value of the magnetic field felt by the nucleus by an amount proportional to the local electronic susceptibility χ_i

$$K_j = \sum_i A_{ij} \chi_i. \tag{16}$$

K_j depends on the position of the nuclei in the unit-cell through the dipolar sum

$$A_{ij} \propto -\gamma_e \gamma_n \hbar^2 \frac{1 - 3\cos^2 \theta_{ij}}{|r_{ij}|^3} \tag{17}$$

where θ_{ij} is the angle between $\boldsymbol{r}_{ij}$ and $\mathbf{H}$. K_j will be positive if $\boldsymbol{h}_j$ is mostly parallel to $\mathbf{H}$, and negative if its antiparallel. CuHpCl contains 24 protons spins in the unit cell: in the NMR spectrum at 16 T (*i.e.* in the polarized phase) shown in Figure 10, there are indeed 24 resolved lines. Their position depends on temperature and follow the T-dependence of the local magnetization. For 16 nuclei the hyperfine shift K_j is positive and negative for the 8 remaining. For proton sites which are nearly equivalents, the lines are close together as the local fields (and their fluctuations) are nearly identical. Using the proton positions calculated from X-ray data, it is possible to determine the dipolar sum on each site and assign it to a corresponding line. For example, the outermost line labeled I arise from nuclei H_{14} and H_{23} ($A_I \approx 2950$ G) while line II arise from proton H_2 ($A_{II} \approx -2400$ G).

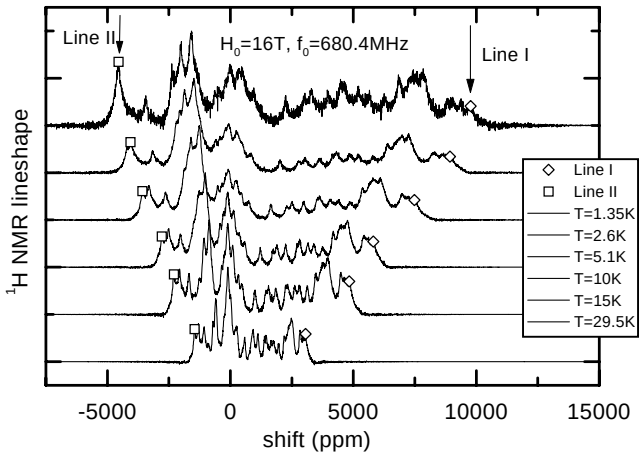

Fig. 10. Temperature dependence of the NMR spectrum measured at 16 T. The intensities have been normalized to compensate for the gap suppression. Most T_1^{-1} measurements have been carried out on Line I and II, which are always located at the extremities of the spectrum for all fields and temperatures. They can be identified with nuclei H_{14} and H_{23} (line I) and nuclei H_2 (line II).

The hyperfine shift is also a measure of the local electronic spin susceptibility M_j/H. Its temperature dependence is shown in Figure 11. Below H_{c1} there is, at low temperature, an exponential drop of the hyperfine shift consistent with an activated behavior with a characteristic energy gap Δ_-. The dependence observed at 8.7 T, just above H_{c1}, shows an increase of the local magnetization as the temperature is raised, a very unusual behavior for a magnetic phase (*e.g.* the magnetization of canted antiferromagnets always decrease with temperature). At low temperature ($k_B T < J_\perp$) it is meaningful to use the XXZ representation, where the system can be viewed as a Luttinger liquid of triplets: in this limit, the presence of a continuum of longitudinal excitation carrying an angular momentum $\hbar$ (see Sect. 4) contributes to an increase of the triplet occupation with temperature. At higher fields, the density of states at small wavevectors gets smaller and a more classical behavior is recovered. In quantitative term, the hyperfine shift observed below 6 K $\approx J_\perp/2$ agrees well with the XXZ mapping and the thermodynamic measurements of M/H (see Fig. 11).

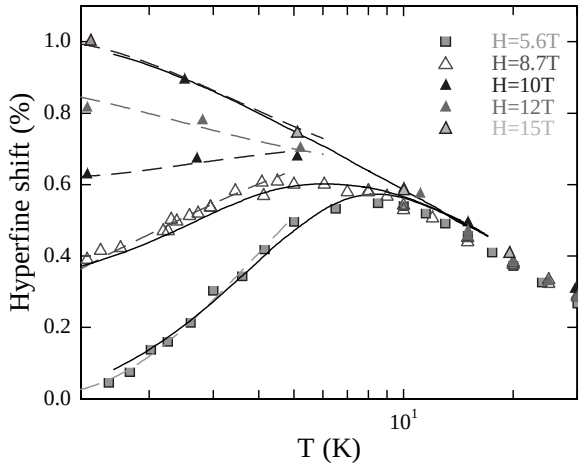

Fig. 11. Temperature dependence of the hyperfine shift at different magnetic fields. The thermodynamic measurement of M/H at H = 5, 8 and 15 T are plotted on the same graph as solid lines. The comparison of the NMR shift to the value of M/H inferred from the *XXZ* mapping (Sect. 4) at low temperature are drawn as dotted lines. At 8.7 T, in the gapless *XXZ*-phase, there is first an increase of the local magnetization with temperature, an unusual behavior for a magnetic state.

Temporal fluctuations of the local fields $\boldsymbol{h}_{ij}(t)$ at the nuclear precession frequency (essentially zero energy) provide the dominant relaxation channel for nuclear spins. The longitudinal spin-lattice relaxation rate of the nucleus i

$$\left.\frac{1}{T_1}\right|_i = \int \exp(-i\omega_n t)dt \sum_j \langle h^+_{ij}(t)h^-_{ij}(0)\rangle \qquad (18)$$

$$= \frac{(\gamma_n\gamma_e\hbar)^2}{2}\sum_q \left[F^i_\perp(q)\mathcal{S}_\perp(q,\omega_n) + F^i_z(q)\mathcal{S}_z(q,\omega_n)\right] \qquad (19)$$

is sensitive to the transverse *and* longitudinal structure factors

$$\mathcal{S}_\perp(q,\omega_n) = \int \exp(-i\omega_n t)dt\langle S^+_q(t)S^-_{-q}(0)\rangle, \qquad (20)$$

$$\mathcal{S}_z(q,\omega_n) = \int \exp(-i\omega_n t)dt\langle S^z_q(t)S^z_{-q}(0)\rangle \qquad (21)$$

through the form factors F^i_z and $F^i_\perp$. These quantities are simply the Fourier transform of $|A_{ij}|^2$ defined in equation (17). They are most easily computed in real space as geometrical dipolar sums: the longitudinal and transverse components of the resultant local field on site i, $\boldsymbol{h}_i = \sum_j \boldsymbol{h}_{ij}$, depend on the actual position of the nucleus i in the unit cell. Depending on the proton site selected, the relative magnitude of the form factors F^i_z and $F^i_\perp$ can change by one order of magnitude: this provides a unique way to measure separately *all* components of the structure factor at $\omega = \omega_n$.

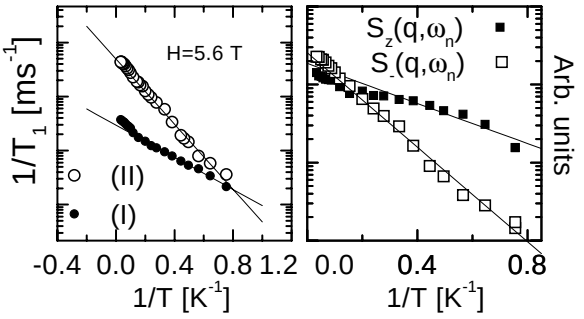

Fig. 12. Temperature dependence of the T_1^{-1} relaxation rate of sites I and II in the gapped phase ($H = 5.6$ T). At high temperature the relaxation at site II is an order of magnitude faster than at site I, but decreases exponentially at lower temperature with an activation energy $\Delta_{II} \approx 6.8$ K, twice as large as for site I, $\Delta_I \approx 3.4$ K.

Figure 12 illustrates how different the relaxation on different proton sites can be in the gapped phase ($H = 5.6$ T). If the T_1^{-1} behavior of both lines I and II are activated, the activation energy for line II, $\Delta_{II} \approx 6.8$ K, is twice as large as the activation energy for line I, $\Delta_I \approx 3.4$ K. In a field of 5.6 T, the smallest activation energy is $\Delta_- = \Delta - g\mu_B H \approx 3.0$ K between the triplet branch $|1,q\rangle$ and the ground state, close to the measured energy Δ_I for line I.

The contribution of one-magnon states $|1,q\rangle$ (*cf.* Eq. 7) to the structure factor are proportional to $\delta(\omega - E_1(q))$: their spectral weight at the nuclear frequency is zero. On the other hand, these states are by no-means exact eigenstates and a number of low-energy scattering processes between magnons can generate a finite spectral weight at low energy. Among them, there are (i) finite matrix elements of $\mathcal{H}_2$ between triplet states which are ignored in the reduction to the effective Hamiltonian $\mathcal{H}_2$, (ii) density-density interactions (last term in Eq. (3)), which contribute as the square of the density of thermally excited magnons, (iii) other interactions such as interchain couplings and impurity scattering.

It is instructive to follow the classification of low-energy processes proposed by Sagi and Affleck [37] in the context of Haldane $S = 1$ spin-chains. Only three relevant channels need to be examined:

(i) The simplest processes are the spin-conserving two-magnons processes (intrabranch) represented in Figure 13: the magnons states $\pi - q/2$ and $\pi + q/2$ within a magnon branch of a given m_z are coupled by the hyperfine interaction which relaxes the nuclear spins. At low temperature, only states in the $m_z = -1$ branch are thermally occupied with a density $\propto \exp(-\Delta_-/k_BT)$. This occupation factor dominates the temperature dependence of this relaxation channel. In this limit, this process contributes to the longitudinal structure factor $\mathcal{S}(\omega_n \approx 0, q \approx 0)$ (no spin-flip).

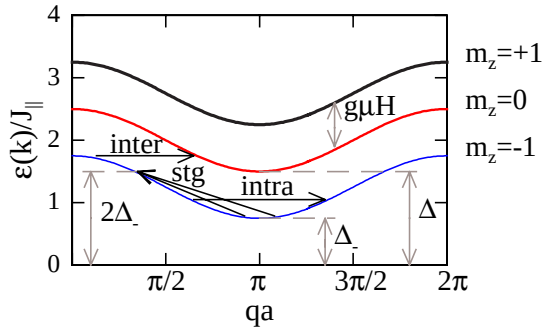

Fig. 13. Schematic representation of multi-magnon scattering processes which can drive the NMR relaxation. The intrabranch processes leave m_z unchanged and contribute only to $\mathcal{S}_z$. The interbranch process which involve a spin flip, contribute to $\mathcal{S}_\perp$ and are quenched one the Zeeman energy (7.6 K at 5.6 T) exceed the triplet bandwidth ($2J_\parallel \approx 5$ K). In the staggered process, two magnons from the bottom of the band -1 are scattered into a magnon state at twice the energy: it is governed by the square of the magnon density $n_-^2 \propto \exp(2\Delta_-)$.

(ii) The spin non-conserving processes (interbranch) couple magnons with energies $> \Delta$ in the $m_z = 0$ and $m_z = -1$ branches. They contribute to the transverse structure factor (there is a spin-flip), with an activation energy set by the full gap Δ. When the Zeeman energy exceeds the one-magnon bandwidth ($2J_\parallel$), which is the case at 5.6 T, this process is completely quenched since there are no states left in $m_z = 0$ and the $m_z = -1$ branches with the same energies.

(iii) Since the magnons states used do not constitute a real representation for the eigenstates of the full Hamiltonian, various processes quadratic in the magnon-density can occur. The lowest order process contributing to the transverse structure factor is a three-magnon process where two-occupied magnons at the bottom of the $m_z = -1$ band are scattered into a magnon with twice the energy *via* a large momentum transfer. The extra angular momentum being absorbed by the nuclear spin, this process contributes to the transverse structure factor $\mathcal{S}_\perp(\omega_n \approx 0, q)$, where q is large and will be taken as π in the rest of the analysis. This process is governed by a quadratic thermal occupation factor $\propto n^2 = \exp(-2\Delta_-/k_BT)$ and requires to have a final state in the $m_z = -1$ branch available at energy $2\Delta_-$: this is the case when the bandwidth $2J_\parallel$ exceeds the gap $\Delta-$, *i.e.* sufficiently close to H_{c1}. There are other relevant quadratic processes: four magnons scattering (Eq. (3)) processes at the bottom of the $m_z = -1$ band have the same temperature dependence but are spin-conserving and hence enter only in the longitudinal structure factor.

To summarize, the dominant processes in an intermediate field range are:
- For the longitudinal structure factor $\mathcal{S}_z$, the intrabranch two-magnon process, $\mathcal{S}_z \propto n_- \propto \exp(-\Delta_-/k_BT)$.

Table 1. The form factors for lines I and II, computed as dipolar sums, are expressed in units of 10^{-4}Å^{-6}. The uncertainties which are of the order of 20% -30% have a number of origins and are discussed elswhere [3].

	$F_z(0)$	$F_\perp(\pi)$
Line I	13	6
Line II	4	70

- For the transverse structure factor $\mathcal{S}_\perp$, the 3-magnons staggered process represented in Figure 13, $\mathcal{S}_\perp \propto n_-^2 \propto \exp(-2\Delta_-/k_BT)$.

In this simple picture, two numbers $\mathcal{S}_z(q = 0)$ and $\mathcal{S}_\perp(q \approx \pi)$ are sufficient to specify the T_1^{-1} relaxation of all lines at a given field and temperature

$$\left.\frac{1}{T_1}\right|_i \propto F_z^i(0)\mathcal{S}_z + F_\perp^i(\pi)\mathcal{S}_\perp. \qquad (22)$$

The value of the form factors F appropriate for line I and II are given in Table 1. Since $F_\perp^{II} \gg F_z^{II}$, line II is dominated by the transverse structure factor, *i.e.* is governed by the staggered processes $\propto \exp(2\Delta_-/k_BT)$ in this field range: this is fully consistent the observed activation energy. While longitudinal and transverse fluctuations contribute to line I, the linear system (22) can be solved explicitly and the different component of the structure factor, plotted in Figure 12, show very clearly the two different activation energies, corresponding to the two dominant processes.

At high temperature, when the thermally excited fermion density is important, the staggered processes dominate by an order of magnitude. Since the fermion density is likewise large above the critical field H_{c1}, staggered processes dominate the relaxation in the XXZ-phase, a result which is consistent with all theoretical analysis [7,10, 37] and the data presented in Figure 15.

The relaxation rate T^{-1} in the polarized phase (above H_{c2}) is also activated as shown in Figure 14. The measured activation energy is close to $g\mu_B(H - H_{c2})$ in good agreement with the exact low energy spectrum described in Appendix A. Hence, this polarized phase has no Goldstone mode and in this sense is not a ferromagnet. There are two magnons modes above the polarized state (two spins per unit cell): hence, the structure of the spectrum above H_{c2} and below H_{c1} is qualitatively different, indicating that the XXZ model which reproduces correctly the low-energy behavior in the gapless phase, cannot be taken literally over the entire phase diagram.

7 Incommensurate phase and quantum critical regime

Figure 15 gives the overall temperature and field dependence of the NMR relaxation rate (line I) through the entire phase diagram. In the left panel, the dependence of the T_1^{-1} rate through the lower critical field is displayed.

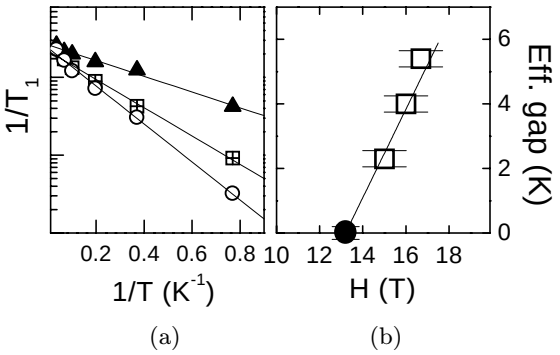

Fig. 14. (a) Activated behavior of T^{-1} (line I) in the high field phase. (b) Effective gap as a function of magnetic field. The intercept on the field axis coincide with the value of $H_{c2} = 13.2$ T.

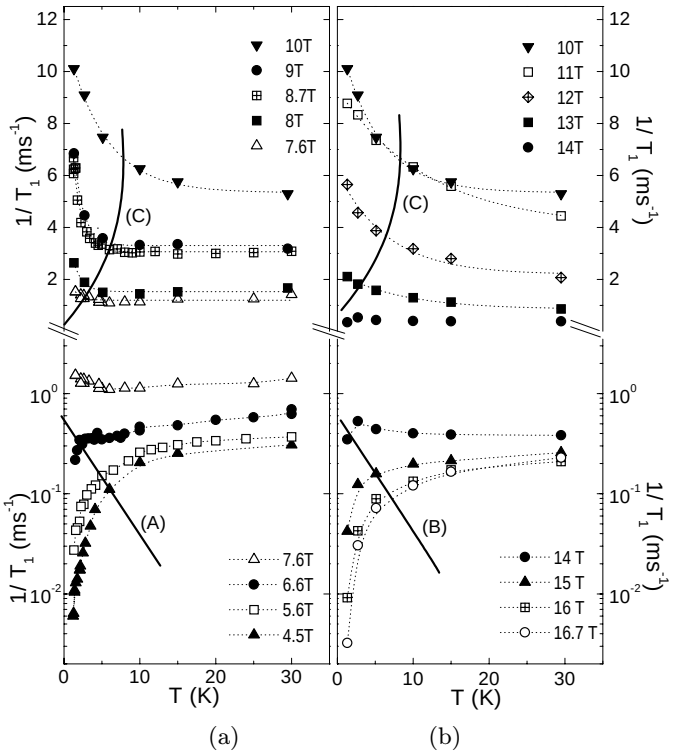

Fig. 15. (a) Temperature dependence of $1/T_1$ through the critical field H_{c1}. In the lower part, the T_1^{-1} dependence in the singlet gapped phase ($H < H_{c1}$) is displayed, while its behavior in the magnetic phase ($H > H_{c1}$) is shown in the upper part. The dashed lines are guides to the eyes. Lines labeled (A) and (C) correspond to the crossover lines of Figure 1. (b) Temperature dependence of $1/T_1$ through the critical field H_{c2}. The upper part shows the behavior in the magnetic phase below H_{c2} while the lower part is in the "fully polarized" gapped phase ($H > H_{c2}$).

In the lower part, the behavior in the gapped phase is reproduced over a broader temperature range. Two distinct regimes can immediately be recognized. When the temperature is raised at constant field through the effective gap Δ_-, the exponential suppression of the T_1^{-1} crosses over to the temperature independent value of the relaxation rate expected in a classical system. Comparing with Figure 1, this crossover can be recognized as line (A) (defined as $k_B T = \Delta_-$) separating the gapped phase, controlled by quantum fluctuation, and the quantum critical phase where ξ_T is the only relevant lengthscale. When the field is raised above H_{c1}, the behavior at high temperature is qualitatively the same but at low temperature T_1^{-1} starts to diverge. Again, it is possible to place a crossover line (C) separating the two regimes. At high temperature, one recognizes the same quantum critical phase controlled solely by thermal fluctuation, while at low temperature, the spectrum of low energy fluctuation in the gapless magnetic phase controls the NMR relaxation. When the magnetic field is raised and crosses H_{c2} (Fig. 15b), the same features are qualitatively observed, with possibly a weaker divergence of T_1^{-1} at low temperature in the gapless phase. What is the origin of this critical behavior of T_1^{-1} throughout the gapless phase?

Because of the broken rotational symmetry, transverse ($\mathcal{S}_\perp$) and longitudinal fluctuations ($\mathcal{S}_z$) involve different processes (*cf.* Sect. 6) which do not have the same temperature dependence. Since staggered processes, entering $\mathcal{S}_\perp$, were found to dominate the T_1^{-1} just below H_{c1}, it is natural to first examine the transverse low energy modes in the gapless phase. In the XXZ mapping for strongly coupled ladders (Sect. 4), two soft modes (transverse in the valence bond $\uparrow, \downarrow_{-1}$ basis) were found (Fig. 5). One mode is always at $Q = \pi$, and generates the staggered process which was already found to be strongly relevant. The other mode is at an incommensurate wavevector $Q_\sigma = \pi\sigma$, which is near π when H is close to H_{c1} (Fig. 5a). In [10], it was argued that this mode was gapped and did not contribute to transverse spin-spin correlation, in apparent contradiction with the spectrum of the XXZ model discussed in Section 4. On the other hand, this incommensurate soft mode in this model is a transverse singlet-triplet wave. For physically obscure reasons, the transverse spin-spin correlator in this state is indeed found to have zero spectral weight at the incommensurate wavevector. This point is crucial since it introduces a fundamental difference between spin-ladders and integer spin-chains which otherwise belong to the same universality class. This has also important consequences for neutron-scattering studies of spin-ladders. For NMR, the staggered process ($Q = \pi$) becomes the only relevant soft mode for (transverse) relaxation. If the temperature exceeds the maximum of the lower edge of the spectrum[2] between $Q_\sigma = \pi\sigma$ and π (Fig. 5a), many additional modes contribute to $\mathcal{S}_\perp$. Hence the $Q = \pi$ soft mode is only relevant for temperature below the spin-stiffness constant ρ_s,

$$\rho_s \equiv \frac{\pi}{2} J_\parallel \frac{M}{M_{sat}} \approx \sqrt{J_\parallel g \mu_B (H - H_{c1})}, \qquad (23)$$

[2] This quantity is proportional the spin-stiffness of the antiferromagnetic magnons.

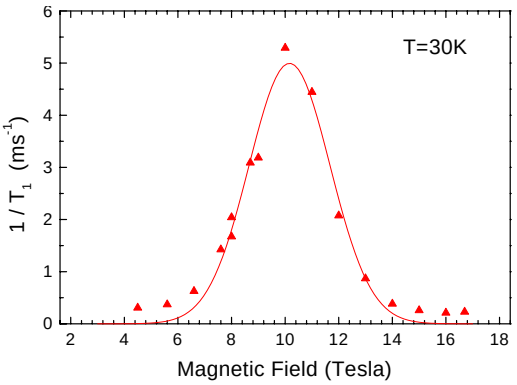

Fig. 16. Field dependence of the longitudinal relaxation rate T_1-1 as a function of magnetic field. The maximum at 10 T is an independent measure of $J_\perp$.

where the approximation is valid close to H_{c1}. The condition $kT \approx \rho_s$ specifies the crossover line between the "Luttinger liquid" and the quantum critical regime (Figs. 1 and 15, line C). As the temperature is lowered, the spectral weight in the $Q = \pi$ soft mode increases giving the divergent contribution to

$$\left.\frac{1}{T_1}\right|_\perp \propto \left(\frac{\rho_s}{k_B T}\right)^{\eta-1}, \qquad (24)$$

where η is the exponent governing the power law decay of the correlation functions [10]. At H_{c1} and H_{c2}, the exponent η is known to be $\eta = 1/2$ [7] and depends smoothly on the magnetization in between. The precise dependence of η with H is not known for ladders and could differ from Haldane systems [38], where the incommensurate mode at Q_σ is relevant. The experimental T_1^{-1} divergence observed at low temperature appears to be fully consistent with a square-root singularity (see Fig. 18). While there could also be additional critical fluctuations associated to the 3D ordering[3] occurring at very low temperature, the divergence of T_1^{-1} which is clearly noticeable below 5 K ($\equiv 2J_\parallel$) has to involve 1D fluctuations.

At temperature above ρ_s, the relaxation rate gradually crosses over to a constant. This high temperature limit of the relaxation rate has a maximum around 10 T, field at which $g\mu_B H \approx J_\perp$.

In classical NMR theory [41], the high temperature limit of the T^{-1} relaxation rate is proportional to the second moment of the spectral distribution of excited states. This quantity is peaked precisely in the middle of the triplet band ($m_z = -1$). At high temperature where dimers are decorrelated, it is thereore natural to find a maximum in the relaxation rate as a function of field (shown in Fig. 16) at the level crossing between the $|-1\rangle$ and $|\uparrow\rangle$ states. Since this "classical" contribution is proportional to the zero frequency spectral weight, its temperature dependence is expected to be weak. It is anyway unrelated to the hydrodynamic soft mode at $Q = \pi$, which is a manifestation of the quasi long-range correlation along the ladder.

The longitudinal fluctuations ($\mathcal{S}_z$) have also a contribution to the T_1^{-1} relaxation rate originating from the $Q = 0$ uniform mode. They have been shown to be non-critical [10]

$$\left.\frac{1}{T_1}\right|_\parallel \propto \frac{k_B T}{\rho_s}. \qquad (25)$$

Since this contribution is noticeable only close to H_{c1}, where it is weak (see Fig. 15), it will not be discussed further.

Since in the experimental data shown in Figure 15, we are clearly able to identify the scaling parameters $x_< = \Delta_-/k_B T$ for $H < H_{c1}$ and $x_> = \rho_s/k_B$ for $H > H_{c1}$ (line A and C) on each side of the critical field, it is natural to construct the scaling plots appropriate to this quantum critical point.

8 Scaling plots in the quantum critical regime

The concept of scaling at a quantum phase transition, one of the most beautiful idea in condensed matter physics, was developed in the context of the metal-insulator transition in disordered systems [42], where it has been brilliantly applied to doped semiconductors [43]. But it is in two-dimensions that the concept has found the most spectacular applications: disordered superconducting films [44, 45] go directly from a superconducting to an insulating state through a $T = 0$ quantum phase transition as a function of disorder. Josephson-junction arrays have a field tune vortex delocalization transition at a critical fraction of the flux quantum f_c [46]. In a two-dimensional electron gas, the transitions between quantum Hall plateaux or to a Hall-insulating state [47] are also governed by zero temperature fixed points [9]. More recently, the scaling properties of a novel metal-insulator transition [48] in silicon MOSFET's have also been thoroughly investigated. In light of this, it is surprising to find so few experimental studies [49] of quantum phase transitions in one dimension. On the other hand, many 1D systems have Lorentz invariance: this confers unique properties to their quantum critical points. In particular, their zero temperature critical behavior can be extended to any temperature *via* conformal mapping [7]. This enables to give a precise description of the finite temperature "quantum critical regime" discussed in the introduction, which is most easily revealed by a scaling analysis.

In the last section, the scaling parameters $x_> = \rho_s/k_B$ and $x_< = \Delta_-/k_B T$ above and below H_{c1} have been identified using NMR. They are also appropriate to scale the magnetization curves (shown in Fig. 7): the resulting plot is shown in Figure 17. Considering the overall quality of the scaling, the variable $x_<$ and $x_>$ are appropriate to this quantum critical point. Furthermore, the 0.42 K curve which crosses into the ordered phase just above H_{c1} can also be included in this plot.

[3] Considering that the $Q = \pi$ magnons in the 3D ordered structure proposed in Section 4 are essentially the same modes as in the 1D quantum disordered phase, the ordering should not have a dramatic effect on the divergence of the NMR rate.

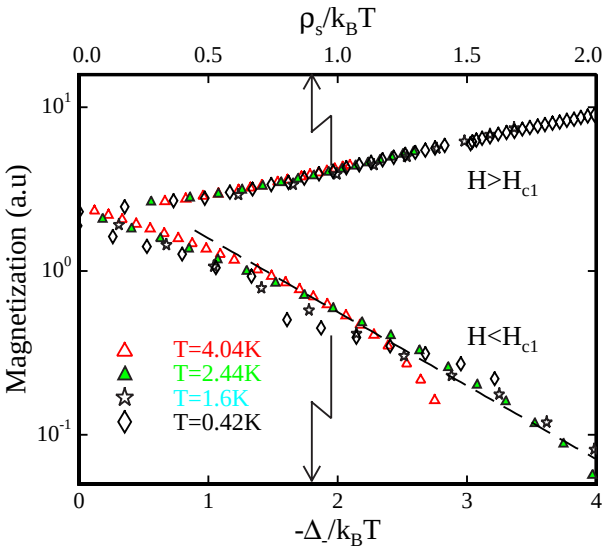

Fig. 17. Magnetization scaling plot. Below H_{c1} all curves collapse on a single curve when plotted in terms of the dimensionless scaling variable $(\Delta - g\mu_B H)/k_B T$. As expected, the straight line with slope -1 for $x > 1$ reproduces the exponential suppression of the magnetization with an effective gap Δ_- at low temperatures. Above H_{c1}, the scaling is also excellent (even in the ordered phase) using the parameter $\frac{\rho_s}{k_B T} = \frac{\sqrt{g\mu_B (H-H_{c1}) J_\parallel}}{k_B T}$.

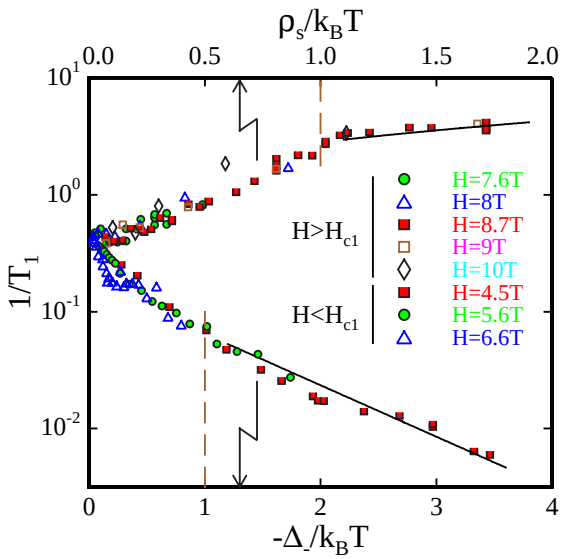

Fig. 18. Scaling plot. Below H_{c1} all the T_1^{-1} measurements collapse on a single curve when plotted in terms of the dimensionless scaling variable $(\Delta - g\mu_B H)/k_B T$. The point $x = 1$ delimits the quantum critical regime from the quantum disordered phase. For $x > 1$, the straight line with slope -1 drawn reproduces precisely the exponential suppression of the T_1^{-1} rate. Above H_{c1}, after subtraction of a constant $C(H)$ to the T_1^{-1} rate, it is possible to scale the remaining critical contributions to the T_1^{-1} relaxation in terms of the scaling variable $\frac{\rho_s}{k_B T} = \frac{\sqrt{g\mu_B (H-H_{c1}) J_\parallel}}{k_B T}$. In the Luttinger liquid regime ($x > 1$), the data is consistent with a scaling function $R(x) = \sqrt{x}$ (solid line).

A similar scaling analysis of the longitudinal relaxation rate is also possible. Below H_{c1}, it is straightforward to scale all the experimental $T_1 - 1$ curves in terms of the single parameter $x_<$, as shown in Figure 18 (lower curve). On this plot, the crossover line (A) shown in Figures 1 and 15 reduces to the single point $x = 1$. For $x > 1$, the exponentially activated behavior with energy Δ_- is the straight line shown with slope -1. Although all curves scale nicely for all x, the quantum critical regime is in principle limited to $k_B T \leq 2J_\parallel$. Above H_{c1}, the appropriate scaling function is harder to construct because there are noncritical (classical) contributions to T_1^{-1} which need to be subtracted. For all data shown in Figure 15, these contributions were determined so that all curves have, after subtraction, the same asymptotic limit at high temperature. The field dependent constant $C(H)$ substracted was chosen to coincide with the single high-T value of T_1^{-1} observed in the gapped phase ($H < H_{c1}$, $T \to \infty$) and is close to the high temperature limit of $T_1 - 1$ plotted in Figure 16. In this way the $T \to \infty$ limit coincides with the $x_< = x_> = 0$ point of the two scaling functions (above and below H_{c1}). After subtraction, all data for $H > H_{c1}$ also collapse on a unique scaling curve when expressed in terms of the scaling parameter $x_>$. Data points with $x > 1$ are in the Luttinger liquid regime and a square-root divergence for T_1^{-1} (line shown) agrees well with the experimental data. The precise scaling function can in principle be constructed for all x from the zero temperature dynamics [6] and compared to this experimental scaling plot.

9 Conclusions

In this work, several clean experiments on spin-ladders have been used to illustrate the physics of quantum phase transitions. Much physical insight could be drawn using a mapping of strongly coupled ladders on a much studied model of quantum magnetism, the XXZ model. For a simple ladder, the anisotropy $\delta = J_z/J_x = 1/2$ puts the system in the planar $(X-Y)$ universality class between the critical fields H_{c1} and H_{c2}. Any frustrating coupling (antiferromagnetic cross-bonding between legs) increases δ. When $\delta > 1$, the interactions between fermions (triplets bonds $\bullet\!\!-\!\!\bullet_{-1}$) are very large and the system switches over to an Ising universality class with long range order. When an Ising gap is present, plateaux appear in the magnetization curve in the vicinity of $H_{eff} = 0$ ($\Leftrightarrow H = (H_{c1} + H_{c2})/2$, half filling), as the magnetic field has to overcome the Ising gap induced by the interactions. This problem has also been investigated theoretically by more general means [50]. An interesting possibility raised in this paper is that similar physics could be induced by much smaller 3D antiferromagnetic coupling and may already have been observed in specific heat experiments [30,31] on CuHpCl.

In the incommensurate gapless phase, low energy dynamical properties are dominated by the $Q = \pi$ soft mode in the transverse excitation spectrum (*cf.* Fig. 5). These fluctuations are not completely quenched

in the gapped phase, since a three-magnons process, which can easily be identified by the temperature dependence of the NMR relaxation rate [3], remains very strong close to H_{c1} ($T_1^{-1} \propto \exp(-2\Delta_-/k_BT)$). At finite temperature, spin-flip processes introduce a natural cutoff of the spin-spin correlations. When k_BT is larger than a characteristic quantum energy (the effective gap Δ_- below H_{c1} or the spin-stiffness ρ_s above H_{c1}), spin correlation have the same nature: this is the quantum critical regime [6]. All dynamical properties have in this limit a universal behavior which should be common to quantum phase transition in 1D with a continuous symmetry. The scaling properties of the NMR relaxation data on CuHpCl [4] analyzed in this work should serve as a reference for future studies of 1D quantum critical points.

In spite of this almost idyllic picture, some questions remain open. In the gapless phase, the incommensurate soft mode should have observable consequences, probably requiring different experimental probes than the ones considered here. The nature of the low temperature ordered phase appears to hold the answer to several key issues in strongly correlated systems. One question to be answered is: can 1D quantum correlation persist in some form in 3D ordered phases? Finally, other compounds with more frustrated magnetic structures can potentially open new horizons in quantum magnetism: for example, there are new universality classes which have not been considered so far. There are indeed known models [51] exhibiting an energy gap between singlet and triplet sectors but no gaps in the singlet sector. The experimental realization of such systems represents a unique challenge in this field.

The GHMFL is a "Laboratoire Conventionné aux Universités J. Fourier et INPG Grenoble I".

Appendix A: Upper critical field

The energy of the fully polarized state $|f\rangle = |\uparrow,\uparrow,\ldots\rangle$ is

$$E_F = \langle F|\mathcal{H}|F\rangle = N\left(\frac{J_\perp}{4} + \frac{J_\parallel}{2} - g_z\mu_B H\right).$$

The most general state with one unit of angular momentum less than the completely polarized state is

$$|\psi\rangle = \sum_{j=1}^{N}\left(u_j S_{2j}^- + v_j S_{2j-1}^-\right)|F\rangle, \tag{26}$$

where the u_j and v_j are respectively the amplitude on the lower and upper legs. They are specified by the condition that $\psi\rangle$ should be an eigenstate of $\mathcal{H}$ with energy E_-, or equivalently

$$E_F - E_- = \sum_{j=1}^{N}\left[u_j S_{2j}^- + v_j S_{2j-1}^-, \mathcal{H}\right]|F\rangle. \tag{27}$$

This condition yields a set of two coupled equations for the u_j and v_j, which are easily solved in Fourier space. The dispersion relations for the corresponding spin-wave modes $\epsilon^\alpha(k) = E_F - E_-^\alpha(k)$ are

$$\epsilon^o(k) = g_z\mu_B H - J_\parallel(1-\cos k), \tag{28}$$
$$\epsilon^a(k) = g_z\mu_B H - J_\perp - J_\parallel(1-\cos k). \tag{29}$$

In the strong coupling limit, the "acoustic" mode (29) becomes soft first at wavevector $k = \pi$, when the field drops below the field which specifies H_{c2} (12). It is straightforward to generalize the argument to more complex systems.

Appendix B: Thermodynamics of the XXZ model

This problem has been completely set out by Takahashi and Suzuki [33]. For an anisotropy factor of $J_z/J_x = 1/2$, all thermodynamic quantities can be computed from the solution of the coupled set of integral equations for the functions $\eta(x)$ and $\kappa(x)$,

$$\ln\eta(x) = 3\sqrt{3}\frac{J_\parallel}{k_BT} + s(x) * \ln(1+u(x))$$
$$u(x) = 2\kappa(x)\cosh\frac{3g\mu_B H_{eff}}{2k_BT} + \kappa^2(x) \tag{30}$$
$$\ln\kappa(x) = s(x) * \ln(1+\eta(x)) \tag{31}$$

where $s(x) = \frac{1}{4}\mathrm{sech}\frac{\pi x}{2}$ and $*$ is the convolution product of two functions. For each value of the temperature and of the effective field, the thermodynamics is specified by the value $\kappa(0)$, *i.e.* the free-energy per spin is

$$\frac{F}{N} = -\frac{J_\parallel}{4} - k_BT\ln\kappa(0). \tag{32}$$

We solved equation (31) iteratively from the known solutions, $\eta(x) = 3$ and $\kappa(x) = 2$ for $J_\parallel = 0$ and $H_{eff} = 0$. We checked our results against the power series expansion in J/T [33]

$$\frac{F}{N} = -k_BT\ln\left(2\cosh\frac{g\mu H}{2k_BT}\right) - \frac{J}{8}\frac{1}{\cosh^2\left(\frac{g\mu H}{2k_BT}\right)} - \frac{3J^2}{32k_BT}\left\{\frac{1}{\cosh^2\left(\frac{g\mu H}{2k_BT}\right)} - \frac{1/4}{\cosh^4\left(\frac{g\mu H}{2k_BT}\right)}\right\}.$$

The comparison with the experimental results shown in Figure 7 is really excellent.

References

1. F.D.M. Haldane, Phys. Rev. Lett. **50**, 1153 (1983); F.D.M. Haldane, Phys. Lett. A **93**, 464 (1983).
2. G. Chaboussant, P.A. Crowell, L.P. Lévy, O. Piovesana, A. Madouri, D. Mailly, Phys. Rev. B **55**, 3046 (1997).
3. G. Chaboussant, M.-H. Julien, Y. Fagot Revurat, L.P. Lévy, C. Berthier, M. Horvatić, O. Piovesana, Phys. Rev. Lett. **79**, 925 (1997).
4. G. Chaboussant, Y. Fagot-Revurat, M.-H. Julien, M.E. Hanson, C. Berthier, M. Horvatić, L.P. Lévy, O. Piovesana, Phys. Rev. Lett. **80**, 2713 (1998).
5. J.A. Hertz, Phys. Rev. B **14**, 1165 (1976).
6. A.V. Chubukov, S. Sachdev, J. Ye, Phys. Rev. B **49**, 11919 (1994).
7. S. Sachdev, T. Senthil, R. Shankar, Phys. Rev. B **50**, 258 (1994).
8. S. Sachdev, Phys. Rev. B **55**, 142 (1997).
9. S.L. Sondhi, S.M. Girvin, J.P. Carini, D. Shahar, Rev. Mod. Phys. **69**, 315 (1997).
10. R. Chitra, T. Giamiarchi, Phys. Rev. **55**, 5816 (1997).
11. in *Champs, Cordes et Phénomènes Critiques*, edited by E. Brézin, J. Zinn-Justin (Elsiever, 1989).
12. L.P. Lévy in *Magnétisme et Supraconductivité* (Interéditions, 1997), pp. 232-238.
13. G.S. Uhrig, H.J. Schulz, Phys. Rev. B **54**, 9624 (1996).
14. I. Affleck, T. Kennedy, E. Lieb, H. Tasaki, Phys. Rev. Lett. **59**, 799 (1987).
15. K.M. Diederix, H.W.J. Blöte, J.P. Groen, T.O. Klaassen, N.J. Poulis, Phys. Rev. B **19**, 420 (1979).
16. J.P. Renard, M. Verdaguer, L.P. Regnault, W.A.C. Erkelens, J. Rossat-Mignod, W.G. Sterling, Europhys. Lett. **3**, 945 (1987).
17. Y. Ajiro, T. Goto, H. Kikuchi, T. Sakakibara, T. Inami, Phys. Rev. Lett. **63**, 1424 (1989).
18. K. Katsumata, H. Hori, T. Takeuchi, M. Date, A. Yamagishi, J.P. Renard, Phys. Rev. Lett. **63**, 86 (1989).
19. N. Fujiwara, T. Goto, S. Maegawa, T. Kohmoto, Phys. Rev. B **47**, 11860 (1993).
20. E. Dagotto, T.M. Rice, Science **271**, 618 (1996).
21. M. Azuma, Z. Hiroi, M. Takano, K. Ishida, Y. Kitaoka, Phys. Rev. Lett. **73**, 3463 (1994).
22. Z. Hiroi, M. Takano, Nature **377**, 41 (1995).
23. B. Chiari, O. Piovesana, T. Tarentelli, P.F. Zanazzi, Inorg. Chem. **29**, 1172 (1990).
24. C. Hawyard, D. Poilblanc, L.P. Lévy, Phys. Rev. **54**, 12649 (1996).
25. K. Totsuka, Phys. Rev. B **57** 3454 (1998).
26. F. Mila, cond-mat/9805029.
27. M. Reigrotzki, H. Tsunetsugu, T.M. Rice, J. Phys.-Cond. **6**, 9325 (1994).
28. P. Crowell, A. Madouri, M. Specht, G. Chaboussant, D. Mailly, L.P. Lévy, Rev. Sci. Inst. **67**, 4161 (1996).
29. Z. Weihong, R.R.P. Singh, J. Oitmaa, Phys. Rev. **55**, 8052 (1997).
30. P.H. Hammar, D.H. Reich, C. Broholm, F. Trouw, Phys. Rev. B **57**, 7846 (1998).
31. R. Calemzuck, *et al.*, cond-mat/9805237.
32. C.N. Yang, C.P. Yang, Phys. Rev. **150**, 321 (1966); *ibid.* **151**, 258 (1966).
33. M. Takahashi, M. Suzuki, Prog. Theor. Phys. **48**, 2187 (1972); M. Takahashi, Prog. Theor. Phys. **50**, 1519 (1973).
34. M. Troyer, H. Tsunetsugu, D. Würtz, Phys. Rev. B **50**, 13515 (1994).
35. Since all the high-energy states are excluded in the XXZ mapping, its validity is limited to temperatures below the $J_\perp/k_B$ .Similarly, the Zeeman splitting must be sufficiently large (say $g\mu_B H > J_\perp/2$) to avoid admixture with higher energy states.
36. A. Georges, private communication.
37. J. Sagi, I. Affleck, Phys. Rev. B **53**, 9188 (1996).
38. T. Sakai, M. Takahashi, Phys. Rev. B **43**, 13383 (1991).
39. Y. Fagot-Revurat, M. Horvatić, C. Berthier, P. Segransan, G. Dhalenne, A. Revcolecvshi, Phys. Rev. Lett. **77** 1861 (1996).
40. F.H.L. Essler, A.M. Tsvelik, G. Delfino, Phys. Rev. B **56** 11001 (1997).
41. T. Moriya, Prog. Theor. Phys. **16**, 23 (1956).
42. E. Abrahams, P.W. Anderson, D.C. Licciardello, T.V. Ramakrishnan, Phys. Rev. Lett. **42**, 673 (1979).
43. M.A. Paalanen, T.F. Rosenbaum, G.A. Thomas, R.N. Bhatt, Phys. Rev. Lett. **48**, 284 (1982); T.F. Rosenbaum *et al.*, Phys. Rev. B **27**, 7509 (1983); H. Stupp, M. Hornung, M. Lakner, O. Madel, H.v. Löhneysen, Phys. Rev. Lett. **71**, 634 (1993); M.P. Sarachik *et al.*, cond-mat/9706309.
44. D.B. Haviland, Y. Liu, A.M. Goldman, Phys. Rev. Lett. **62**, 2180 (1989).
45. A.F. Hebard, M.A. Paalanen, Phys. Rev. Lett. **65**, (1990) 927.
46. C.D. Chen, P. Delsing, D.B. Haviland, Y. Harada, T. Claeson, Phys. Rev. B **51**, 15645 (1995).
47. D. Shardar, D.C. Tsui, M. Shayegan, E. Shimshomi, S.L. Sondhi, Phys. Rev. Lett. **79**, 479 (1997); T. Wang, K.P. Clark, G.F. Spencer, A.M. Mack, W.P. Kirk, Phys. Rev. Lett. **72**, 709 (1994).
48. S.V. Kravchenko, D. Simonian, M.P. Sarachick, W. Mason, J.E. Furneaux, Phys. Rev. Lett. **77**, 4938 (1996); D. Popovic, A.B. Fowler, S. Washburn, Phys. Rev. Lett. **79**, (1997).
49. D.B. Haviland, P. Delsing, unpublished.
50. D. Cabra, A. Honecker, P. Pujol, Phys. Rev. Lett. **79**, 5126 (1997) and cond-mat/9802035.
51. Ch. Waldtmann, H.-U. Everts, B. Bernu, P. Sindzingre, C. Lhuillier, P. Lecheminant, P. Pierre, cond-mat/9802168.